

Alexandre Perrig
 François Avellan
 Jean-Louis Kueny
 Mohamed Farhat

Laboratory for Hydraulic Machines,
 Ecole Polytechnique Fédérale de Lausanne
 (EPFL),
 CH-1015 Lausanne, Switzerland

Etienne Parkinson
 VATECH Hydro Ltd.,
 Rue des 2 Gares, 6,
 CH-1800 Vevey, Switzerland

Flow in a Pelton Turbine Bucket: Numerical and Experimental Investigations

The aim of the paper is to present the results of investigations conducted on the free surface flow in a Pelton turbine model bucket. Unsteady numerical simulations, based on the two-phase homogeneous model, are performed together with wall pressure measurements and flow visualizations. The results obtained allow defining five distinct zones in the bucket from the flow patterns and the pressure signal shapes. The results provided by the numerical simulation are compared for each zone. The flow patterns in the buckets are analyzed from the results. An investigation of the momentum transfer between the water particles and the bucket is performed, showing the regions of the bucket surface that contribute the most to the torque. The study is also conducted for the backside of the bucket, evidencing a probable Coanda interaction between the bucket cutout area and the water jet. [DOI: 10.1115/1.2170120]

Introduction

Performance prediction of hydraulic machines, such as efficiency and dynamic behavior under different operating conditions, is of high interest to manufacturers. The design of Pelton turbines is mainly conducted from know-how and extensive experimental testing. In today's highly competitive market of turbine upgrading and refurbishment, the performance guarantees are often difficult to determine in the short term. An accurate prediction of Pelton machines by numerical simulation would reduce the time required for the design phase.

Few experimental investigations of the flow in Pelton turbines are presented in the literature. Lowy investigated the flow in a fixed bucket and, more particularly, the cutting process of the jet by the bucket cutout [1], whereas Bachman et al. [2] performed flow visualizations around a Pelton runner. Grozev et al. [3] and Kvicinsky et al. [4] performed pressure measurements in nonrotating Pelton buckets in steady state. Water-layer thickness measurements on static buckets were also performed by Kvicinsky et al. [4] and Guilbaud et al. [5].

In recent years, physical models allowing complex free surface flow modeling have been developed and refined. The main models are the volume of fluid (VOF) method and the two-phase homogeneous model. Kvicinsky et al. [6] investigated both models and experimentally validated them in the cases of a jet impinging a flat plate and a nonmoving Pelton turbine bucket [3]. The two-phase homogeneous model appeared to provide the best results in terms of accuracy and computational cost. The first attempts to numerically simulate the flow in a moving Pelton turbine bucket were conducted by Hana [7], Sick et al. [8–10], Janetzky et al. [11], and Mack and Moser [12].

In the present study, extensive experimental and numerical investigations in a rotating Pelton turbine bucket are presented. The transient wall pressure distribution measured on the bucket inner surface of a runner in rotation permits the validation of the physical models by comparing the corresponding numerical results to the measurements. A procedure for advanced instrumentation of reduced-scale turbine models, developed by Kvicinsky et al. [13] and Farhat et al. [14], is applied for the experimental investigations.

At first, the physical models chosen are detailed. These include

the two-phase homogeneous model in a rotating frame of reference, the free surface, and surface tension modeling. Then, the numerical setup and the experimental techniques are presented. Finally, the results obtained from both approaches are analyzed, compared, and the momentum transfer in the bucket is discussed.

Two-Phase Homogeneous Model

The flow model used for the numerical simulations is based on the generalized homogeneous multiphase flow model developed by Ishii [15], with the additional sources of momentum for the effects of the Coriolis and centrifugal accelerations in a steady rotating frame of reference. The governing equations are described below

Continuity Equation

$$\frac{\partial \rho_m}{\partial t} + \vec{\nabla} \cdot (\rho_m \vec{W}_m) = 0 \quad (1)$$

where the mixture density ρ_m and the mixture relative flow velocity \vec{W}_m are defined as

$$\rho_m = \sum_{n=1}^2 \alpha_n \rho_n \quad \text{and} \quad \vec{W}_m = \frac{\sum_{n=1}^2 \alpha_n \rho_n \vec{W}_n}{\rho_m} \quad (2)$$

where the volume fraction α_n is given by

$$\alpha_n = \frac{V_n}{\sum_n V_n} \quad (3)$$

Momentum Equation

$$\begin{aligned} \frac{\partial}{\partial t} (\rho_m \vec{W}_m) + \rho_m (\vec{W}_m \cdot \vec{\nabla}) \vec{W}_m \\ = - \vec{\nabla} p_m + \vec{\nabla} (\bar{\tau}_m + \bar{\tau}_m) - \rho_m \vec{\omega} \times (\vec{\omega} \times \vec{r}_m) - 2 \vec{\omega} \times \vec{W}_m + \vec{f}_m \end{aligned} \quad (4)$$

where \vec{f}_m represents any body force.

Diffusion Equation. This drives the mass transfer between each phase by assuming that both phases share the same flow field

$$\frac{\partial \alpha_n \rho_n}{\partial t} + \vec{\nabla} \cdot (\alpha_n \rho_n \vec{W}_m) = \Gamma_n \quad (5)$$

Contributed by the Fluids Engineering Division of ASME for publication in the JOURNAL OF FLUIDS ENGINEERING. Manuscript received January 19, 2005; final manuscript received September 8, 2005. Review conducted by Yu-Tai Lee.

Table 1 Operating conditions for the investigated point

Specific Energy	Discharge	Efficiency	Needle stroke
ψ/ψ_{opt} 1.01	ϕ/ϕ_{opt} 1.03	η/η_{opt} 0.999	s/s_{opt} 1.04

The mixture pressure p_m is written as

$$p_m = \sum_{n=1}^2 p_n \quad (6)$$

For keeping the interface as thin as possible, a compressive differencing scheme for the advection of volume fractions and a compressive transient scheme for the volume fraction equations are used according to [16].

The surface-tension model used is based on the continuum surface force model of Brackbill et al. [17]. The surface-tension force is modeled as a volume force concentrated at the interface. The surface-tension force $\vec{F}_{\alpha\beta}$ between a primary fluid α , the liquid phase, and a secondary fluid β , the gaseous phase, is given by

$$\vec{F}_{\alpha\beta} = \vec{f}_{\alpha\beta} \delta_{\alpha\beta} \quad (7)$$

where

$$\vec{f}_{\alpha\beta} = -\sigma_{\alpha\beta} \kappa_{\alpha\beta} \vec{n}_{\alpha\beta} + \vec{\nabla}_s \sigma_{\alpha\beta} \quad (8)$$

and

$$\delta_{\alpha\beta} = \begin{cases} 1 & r_{\alpha\beta} \equiv 0 \\ 0 & r_{\alpha\beta} > 0 \end{cases} \quad (9)$$

The two terms summed on the right-hand side of Eq. (8) reflect the normal and tangential components of the surface tension force. $\delta_{\alpha\beta}$ is called the interface δ function; it is zero away from the interface, thereby ensuring that the surface-tension force is active only near the interface.

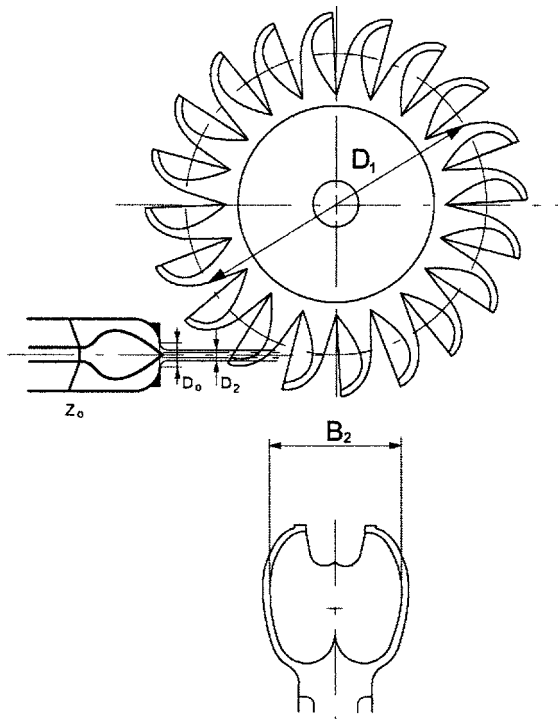


Fig. 1 Single-injector horizontal Pelton turbine

Table 2 Mesh sizes

	Mesh 1 (k)	Mesh 2 (k)	Mesh 3 (k)	Mesh 4 (k)
Number of nodes rotor	70	150	240	608.5
Number of nodes stator	7.5	25	45	76.5
Total number of nodes	77.5	175	285	685

Flow Computation

A single-injector horizontal axis 20-bucket Pelton turbine model of $D_1/B_2=3.5$ is investigated (see Fig. 1). For the purpose of the present analysis, a single operating point (see Table 1), close to the best efficiency point, is considered to avoid any off-design driven phenomena.

The numerical simulation of the flow is carried out with the CFX-5® code. The continuity and momentum equations are discretized using a high-resolution upwind scheme with the physical advection terms weighted by a gradient-dependent blend factor, providing a good trade-off between diffusion and dispersion. A second-order backward Euler scheme is used for the transient terms.

The incoming jet is assumed to be ideal, with a constant velocity profile determined from the specific energy and discharge conditions, and the flow relative to the splitter to be symmetrical. The turbulence is taken into account using a $k-\epsilon$ turbulence model with a standard wall function. No casing is taken into account, and the pressure surrounding the turbine is considered as constant. As far as body forces are concerned, only the surface-tension force acting on the flow is modeled.

The computational domain is divided in two subdomains, i.e., a stator with a dummy injector and a rotor with the runner. By assuming periodic flow, one-quarter of the runner is simulated, i.e., five buckets (Fig. 2). A transient rotor-stator sliding interface is set between the two subdomains. The domains are modeled by an unstructured mesh made of 685 k nodes, i.e., 2.4 million tetrahedral elements.

Quality Check of Numerical Simulation Results

The simulation is run until the rms residuals for the momentum equations reduce below 10^{-5} , and the bucket and runner torques become periodic. The mass flow conservation through the domain is checked as well. In order to check the mesh influence on the solution, four different meshes with an increasing number of elements are tested (see Table 2). Five reference monitoring points, distributed in the bucket inner surface, are selected (see Fig. 4). The rms value of the absolute grid solution error on the calculated

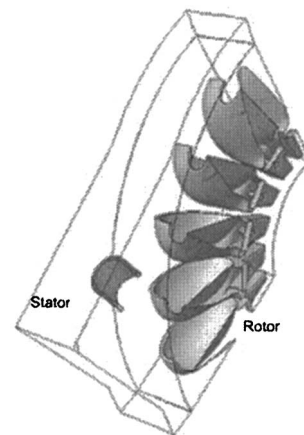


Fig. 2 Computational domain

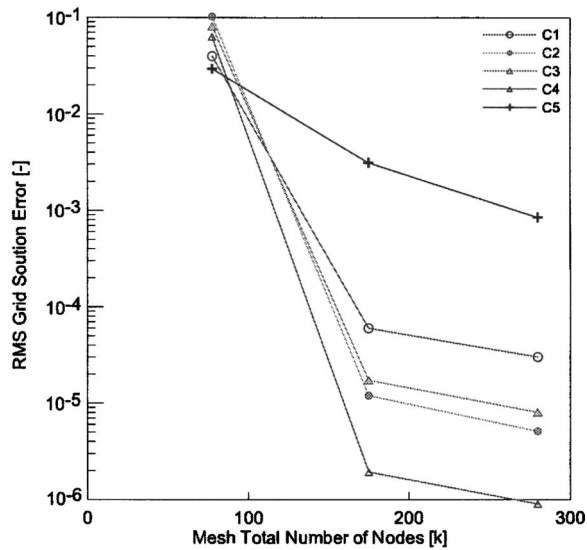


Fig. 3 Influence of mesh size on solution error for the five pressure taps

pressure signal for each monitoring point between the coarse meshes and the finer mesh is determined and plotted in Fig. 3.

$$\text{rms}(\text{error}) = \sqrt{\frac{1}{N} \sum_{i=1}^N \left(\frac{f_{\text{fine}_i} - f_{ki}}{f_{\text{fine}_i}} \right)^2} \quad (10)$$

where f_{fine_i} is the solution on the finest grid and f_k the solution for coarse grid k . The subscript i refers to the time step, and N is the total number of time steps.

The error decreases with the mesh size increase and remains low from 200 k nodes. It appears that no significant enhancement is to be expected from a further refinement of the mesh.

Pressure Measurement Techniques

The reduced-scale Pelton turbine model is instrumented with an onboard acquisition system developed for measuring the unsteady pressure distribution on the bucket inner surface. Thirty-two miniature piezoresistive pressure transducers of 10 bar range, coated with a silicone compound of the same density as water, are embedded in four buckets.

The onboard electronic for signal conditioning is made of 32 preamplifiers and anti-aliasing filters and is installed in the runner

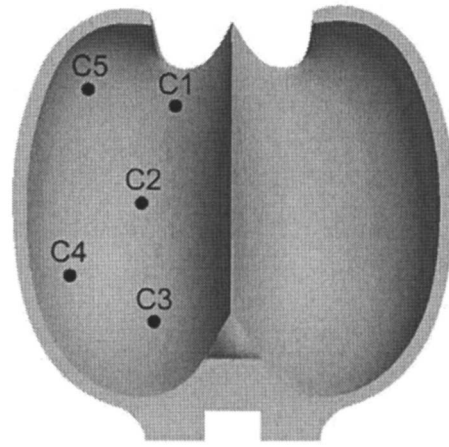


Fig. 4 Locations of the five reference pressure taps on the bucket

shaft (see Fig. 5). The conditioning electronic equipment connected to eight acquisition boards is located in the turbine shaft. Each board has four channel inputs and 12-bit A/D converters. The maximum sampling frequency is 20 kHz, while the memory storage capability is of 64 k-samples per channel. A host computer is used for monitoring purposes via an ArcNet communication network. External communication and power supply are achieved with a four-channel slip ring. The system is capable of transferring up to 1.5 Mbits/s [14]. The synchronization of the data sampling of active boards is performed through a master-slave scheme, all active modules being synchronously triggered within 5 μ s.

The pressure sensor's static calibration is performed by installing the instrumented runner in a pressurized vessel. The measurement error is found to be <0.5% of the measurement range.

The dynamic calibration of the pressure sensors is carried out in a large vessel with a spark-generated bubble device [14]. The pressure-sensor frequency bandwidth extends up to 25 kHz. A check of the sensors is made with the runner spinning in air to measure the effect of centrifugal load.

Data Reduction

In the following sections, the results are presented over one duty cycle of one bucket, referred as bucket j , assumed to be 90 deg [18]. All discussed data, torque, pressure, discharge, and flow visualization stem from the same bucket.

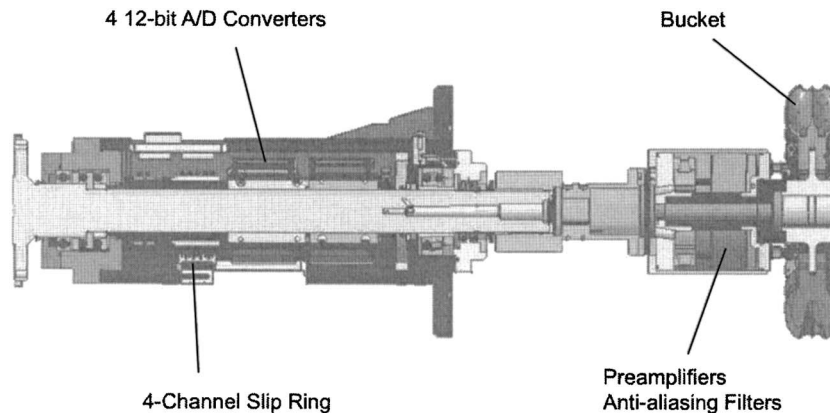


Fig. 5 Instrumentation and data acquisition system installed on the rotating shaft

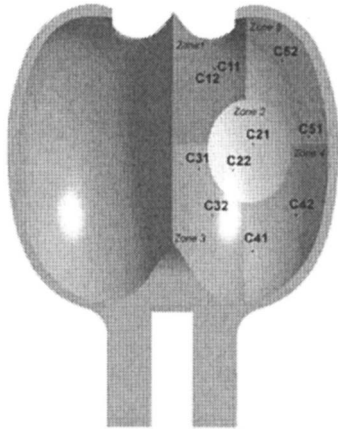


Fig. 6 Definition of the bucket zones with respect to the pressure taps

All the data are presented with respect to the same angular reference. The reference is set as the angular position where bucket j splitter tip is in contact with the jet outer boundary assumed to have remained constant from the injector nozzle. The pressure measurements are phase averaged from 295 runner rotations and synchronized from the tachometric signal.

According to the shape of the phase-averaged transient pressure signals [13,18], the bucket inner surface is divided into five zones of the same surface area, referred as zone 1 through zone 5. Two reference locations for each zone, labeled C11–C52, representative of the local pressure field, are selected for each zone [18] (see Fig. 6).

Numerical Flow Simulation-Measurements Comparison

The results obtained from the measurements and the computations are presented in Fig. 7. The means of comparison are the rise and decay times and slopes, the signal amplitude, the phase shift, and the signal period or duration.

In zone 1, the pressure measurements exhibit either a peak-plateau or a double-peak shape. Rise times are very short, especially in the case of C12. The typical signal for zone 1 can be divided into two portions, ranging, respectively, from 0 deg to 25 deg and from 25 deg to 65 deg duty cycle. In the first portion, the standard deviation remains low, whereas it increases significantly in the second portion, where the second peak, or plateau, is visible. The first portion of the signal is fairly predicted by the simulation in terms of amplitude, with a relative error ranging from 11.5% for C12 to 18% for C11. On the other hand, the signals are well in phase. The rise slope is 35% less in the simulation, and the signal starts earlier. The plateau (see C11) and the second peak (see C12) are barely visible in the numerical flow simulation results, and the calculated period is shorter by 20 deg for C11 and 10 deg for C12.

The pressure signals in zone 2 are in very good accordance between the measurements and the simulation: rise and decay times, signal phases, and signal periods match very well. The predicted amplitude is too high by about 7%. The measured signal exhibits a plateau at maximum amplitude, accounting for 18 deg, i.e., the bucket pitch angle. The measured signal shows a narrow peak of pressure at 12 deg duty cycle. The real amplitude of the peak remains unknown, as its duration is very short, of the order of a few microseconds and the 20 KHz sampling rate too low to capture it adequately. Even if the time step selected for the simulation is three times lower than the experimental sampling rate, the numerical simulation shows a discontinuity for C22. Zone 2 signal accounts for 2/3 of the bucket duty cycle.

In zone 3, the computed amplitudes vary between 7% and 26% below the measured ones. The discontinuity measured by C31 in

the vicinity of 55 deg duty cycle is marked as a change of slope in the simulation, even if the decay slope is underpredicted. For C31, the rise start and the period are in good accordance with the slopes underpredicted, while for C32 the rise and decay slopes are well simulated, but the period is shorter by 6 deg, and the phase shift at signal rise is 2.5 deg.

The numerical flow simulation results for zone 4 underpredict the signal amplitude by more than 15%. For C41, located in the aft region of zone 4, the period is 15 deg shorter than that of the measured signal. The phase shift at signal rise is delayed by 6 deg, while the rise slope is accurately determined. For C42, located closer to the outer edge of the bucket, the period is 8 deg shorter, but the rise is in phase with the measurements.

The signals in zone 5 are well predicted by the numerical flow simulation. Amplitudes for C51 and C52 are very close. Periods are well predicted, but it is remarkable that for C51 the computed signal maximum leads the measurement by 5 deg, while for C52, the maximum of the signal lags them by 6 deg. The differences stated between the numerical flow simulation prediction and the measurements can be explained from the differences between the simulated flow patterns and the real patterns deduced from the available observations and the pressure signals.

Bucket Flow Patterns

The instantaneous bucket discharge functions is computed through a control plane parallel at the tip of bucket j and parallel to the bucket upper edges. Figure 8 shows the instantaneous discharge coefficients entering and leaving the buckets j and $j+1$ during one duty cycle, obtained from the computations. All the angular positions refer to the angular reference defined in the previous section.

The effective discharge coefficient received or released by any bucket can be expressed as

$$\varphi(t) = \frac{4}{\pi B_2^2 U_1} \int_{A_s} \int_0^1 \vec{W}_m \cdot \vec{n} dA d\alpha \quad (11)$$

Inflow. Four stages in the bucket duty cycle can be identified from the kinematics and the inflow discharge function. (i) Cut in: From 0 deg to 14 deg, the jet is progressively cut by the bucket. (ii) Full jet: From 14 deg to 32 deg, the full jet feeds the bucket for an angular duration equivalent to the runner pitch [19]. The jet is actually cut by bucket $j+1$ at 18 deg bucket j duty cycle. However, it is not until 32 deg that the disturbed section of the jet reaches the entry plane of bucket j . The decrease of bucket j discharge observed is due to the change in the relative velocities with the radial displacement of the jet section toward the bucket root [20]. (iii) Cut out: From 32 deg to 46 deg the jet section cut by bucket $j+1$ impinges bucket j . (iv) End of inflow: From 32 deg, the jet is completely separated from the injector, but the remaining portion is still catching up on bucket j . The jet section affected by the complete cut reaches bucket j entry plane at 46 deg duty cycle. From a purely kinematics point of view, the jet should separate from bucket $j+1$ backside, keeping its diameter constant, since the particles of the jet are animated by the absolute velocity C , faster than the runner peripheral velocity. The numerical flow simulation results, on the contrary, show a jet of decreasing diameter that stays attached to bucket $j+1$ backside far in the duty cycle. It is remarkable that the end of the feeding process and, more particularly, the behavior of the cut jet, remain unknown, as no usable observations have been performed thus far on the subject.

For the pressure signal and zone flow analysis to follow, it must be emphasized that there is a phase shift between the entry plane and the position of the sensors on the bucket inner surface, which varies from 3 deg in the cutout area (zone 1) to 8 deg at the bottom of the bucket (zones 2 and 3), depending on the estimated

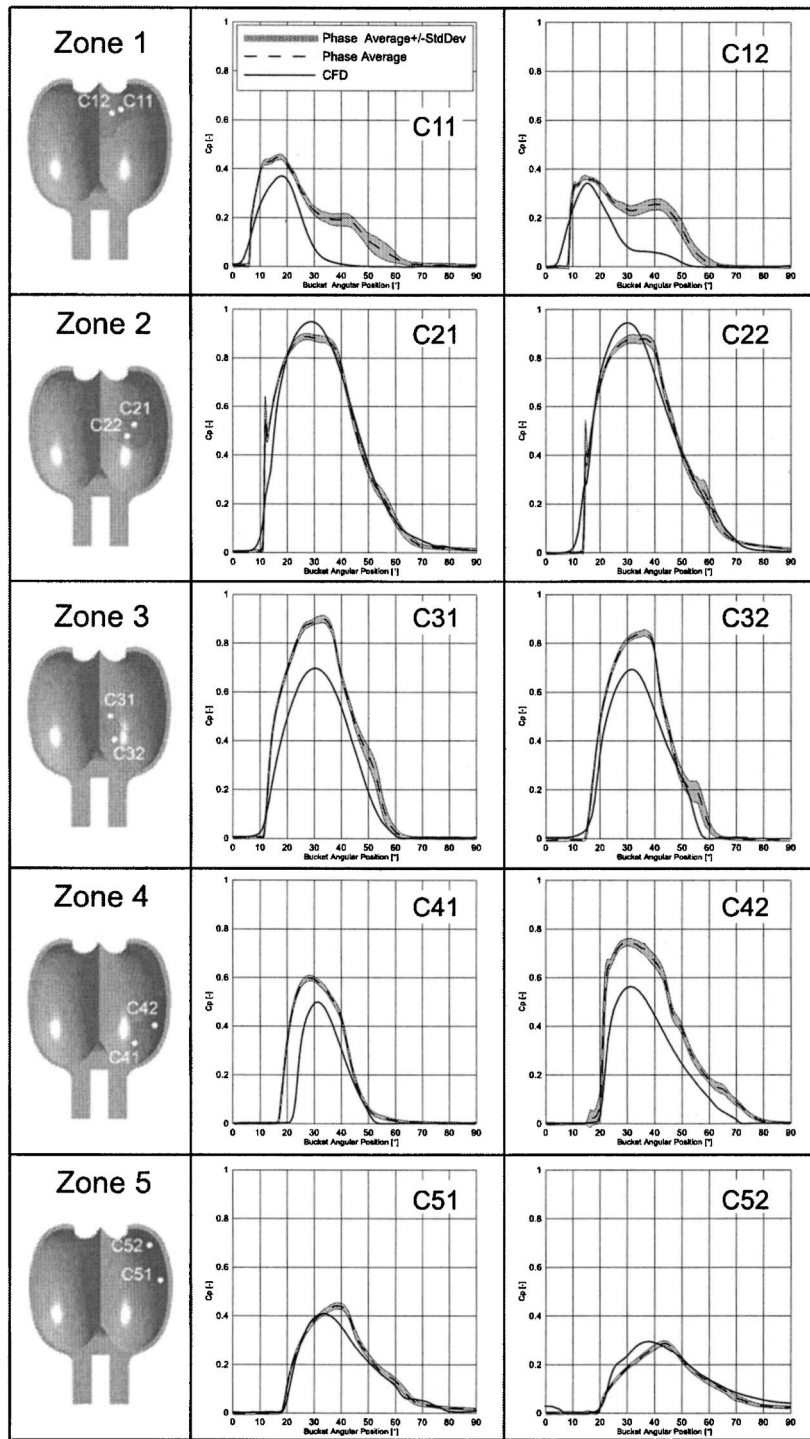


Fig. 7 Comparison of experimental with numerical flow simulation pressure coefficient results

travel time of the water particles from the entry plane. This phase shift has to be taken into account for further analysis.

Outflow. From about 25 deg, the water received at the beginning of the cycle leaves bucket j from the lateral edge, close to its root. The discharge reaches its maximum at the half cycle (45 deg), when the main flow balances from the rear to the outer regions of the bucket. The last drops of water exclusively leave the bucket from the frontal area, near the cutout. The discharge and its radial component decrease never stops, resulting in a line

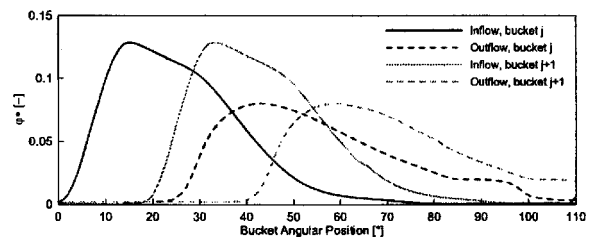


Fig. 8 Evolution of adjacent bucket discharge functions over the duty cycle

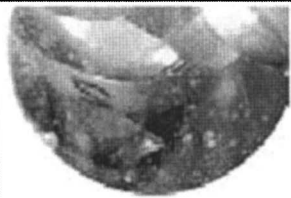
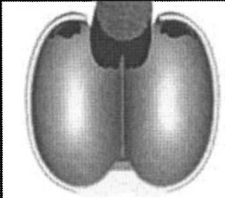
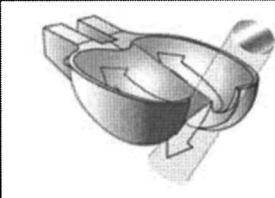

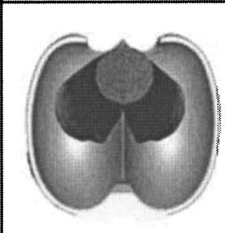
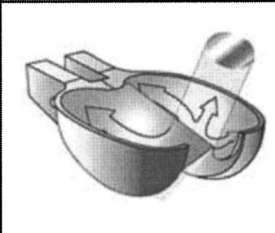
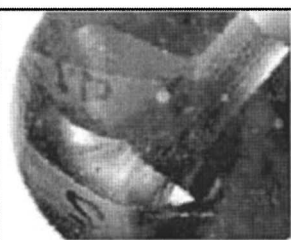
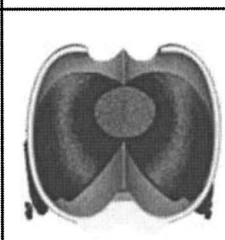
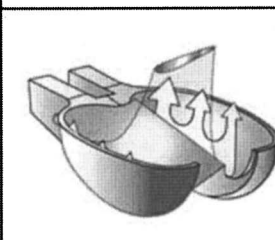
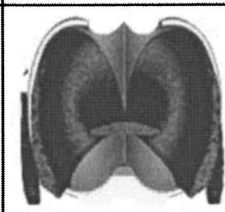
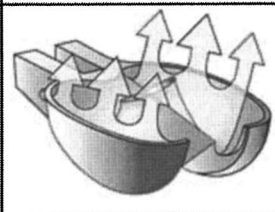


Angular Position	Observations	CFD	Interpretation
0°			
20°			
30°			
45°	N/A		
60°	N/A		

Fig. 9 Evolution of flow pattern along the runner rotation angle

of droplets visible along the entire runner periphery. The evacuation process predicted by the numerical flow simulation is in good accordance with the observations [2].

Flow Analysis

The discussion to follow refers to Fig. 9. The water jet encounters bucket j in zone 1. The first peak of pressure recorded by C11 and C12 sensors is related to the passage of the front of the jet over the sensor. The steep rise slope indicates that the jet interface is sharp, and the small standard deviation confirms the periodicity of the flow. The second peak, or plateau, presents a nonperiodic behavior, as shown by the high standard deviation value. Indeed, three phenomena that are visible from the observations are superposed: (i) As the jet is being cut by bucket $j+1$, after 30 deg, its diameter increases, projecting more water particles on zone 1. (ii) The jet appears to bend toward the bucket j root as the cutting process of bucket $j+1$ starts, modifying its angle of attack relative

to bucket j . (iii) If the flow moves backward in the direction of the bucket root at the beginning of the bucket duty cycle, then it flows toward the cutout, loading zone 1 again in the second half of the duty cycle.

The peak of pressure measured in zone 2 corresponds to the passage of the jet interface over the sensor. It may be related to compressibility effects due to a stagnation point imposed on the flow by the change of bucket surface curvature [13,21]. It is interesting to remark that the area of zone 2 where the peak of pressure is visible often presents erosion damages, even during reduced-scale model testing.

The jet fully feeds bucket j in zone 2 from 20 deg until 38 deg, i.e., the runner pitch. The measured signal remains quasi-steady during the 18 deg pitch period. The flow fills almost the entire bucket helicoidally from zone 2. C21 and C22 account for 5/6 of the bucket duty cycle. The signal shrinks as the feeding process stops. Zone 2 is a focus region that receives water stemming from the whole feeding process. The numerical flow simulation results

for that region are very accurate because the flow received in zone 2 is dominated by inertia effects and is not affected by the jet-bucket interaction.

The short plateau, and a higher-than-average standard deviation at 54 deg duty cycle, visible on the C22 signal may be related with the last section of the cut jet catching up to the bucket, and the transition from jet impact flow to a purely water sheet flow. This would indicate that the feeding process stops earlier than predicted by the numerical simulation.

Zone 3 is where the end of the feeding process occurs. The signal rises are smoother because the front of the jet is not sharp anymore and is preceded by the water sheet already formed in zones 1 and 2. The measured signal for C31 presents a discontinuity at 53 deg duty cycle, followed by a rapid drop of amplitude. This may be related to the last jet section catch-up of the bucket at that instant, as for zone 2. The delay in signal rise may be related to the jet enlargement at the moment of the jet cut stated previously, which is absent in the numerical flow simulation prediction. For C31, the amplitude is underestimated, probably because the flow along the splitter experiences significant shear stresses, for which the standard $k-\epsilon$ turbulence model is probably not valid.

Zone 4 only receives water-sheet flow and is at the beginning of the bucket outflow. The main discrepancies stated in the previous section are the phase shift for C41 and the lack of amplitude of the predicted signals. The predicted sheet of water seems to exhibit a shorter period than the real one, arriving later and leaving the zone earlier. At 15 deg duty cycle, zone 4 is still dry in the numerical flow simulation results, while the measured C41 signal rise indicates that the water sheet already covers zone 4. The predicted water flow trajectory is more laterally deviated than the observed trajectory flowing to the root, bypassing zone 4. The lack of amplitude of the signals is related to the deformation and increase of the diameter stated from the visualizations discussed for zone 1.

From the numerical flow simulation results, the water sheet reaches zone 5 4 deg earlier than zone 4 (see C51 and C52), whereas from the measurements it should be 3 deg late. The accuracy of the prediction is better than in zone 4 because zone 5 is less affected by the deformation and bending of the jet after its encounter with the next bucket.

The main differences that can be stated from the comparison of the experiments and the simulations are as follows: (i) The actual feeding process is faster than predicted by the numerical flow simulation, with more water flowing towards the bucket root, and more water leaving the bucket from zone 4. (ii) The end of the feeding process arises earlier than predicted, between zones 2 and 3, as opposed to the numerical flow simulation, where it arises in zone 3. (iii) The jet enlargement and bending after its encounter with bucket $j+1$ is underestimated in the simulation. (iv) The flow distribution in the bucket: the flow in the buckets balances back and forth, flowing from zone 1 to zone 2 and from zone 2 to zones 3–5 in a counterclockwise pattern [2]. The numerical flow simulation prediction seems to lead the measurements in the first portion of the duty cycle and to lag behind them in the second portion. The jet-cutting process modeling is related to the discrepancies observed. The overall results are accurate enough, however, to draw some conclusions about the power exchange mechanisms involved.

Power Budget

The pressure field does not adequately show where the zones are that contribute the most to the bucket power build up. It is more relevant to investigate the bucket-power history to assess the effective momentum transfer between the flow and the bucket. The critical criteria are as follows: (i) the bucket surface geometry, (ii) the radius of application of the driving force, (iii) the water remaining kinetic energy, and (iv) bucket angle of setting.

The resultant instantaneous power produced by each zone is determined from the projection on the local peripheral direction of the local surface normal pressure of each elementary area A_k that

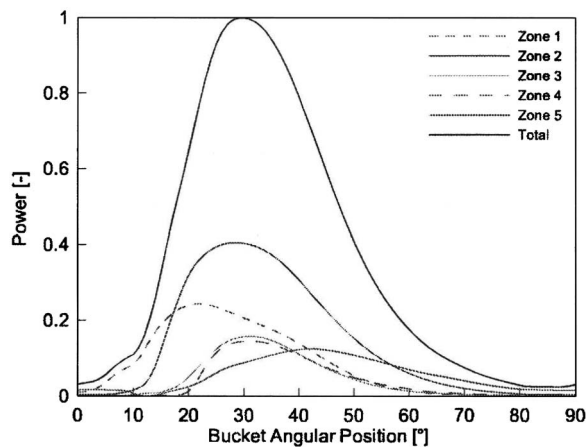


Fig. 10 Contribution of each zone to the total mechanical power exchange as a function of the runner rotation angle. The power is normalized by the total bucket power peak value.

composes zone i , multiplied by the runner angular velocity (see Eq. (12)). The other components of the stress tensor are neglected.

$$P_i = \sum_{k=1}^m \vec{r}_{ik} \cdot \vec{\omega} = \left[\sum_{k=1}^m \vec{r}_{ik} \left(\int_{A_{ik}} p_{ik}(t) \vec{n}_{ik} dA_{ik} \right) \right] \cdot \vec{\omega} \quad (12)$$

The pressure field shows the regions that are the most loaded in terms of normal mechanical stress, but does not give real information about the energy transfer in the bucket. The power contribution of the different bucket regions (see Fig. 10) highlights the effective momentum transfer between the flow and the bucket throughout the bucket period. Zones 1 and 2 contribute the most to the bucket power because these two regions experience the direct impingement of the jet at the beginning of the bucket period, when the kinetic energy of the flow is at its maximum. Zone 2 contributions exhibit the longest and tallest pressure signal, lasting more than 2/3 of the bucket period, and accounts for more than 40% of the bucket torque. Zone 2 can be considered as a focal region, which collects all the water particles transiting in the bucket. The flow received in zone 2 during the full jet period is in accordance with the kinematical assumptions made to design the buckets. This explains why the classic design methods permit one to obtain machines of fair efficiency. The maximum power is reached at 30 deg when the contributions of zones 2–4 are at their respective maximums. The first flow particles, which arrived with the highest kinetic energy, are leaving the bucket at that instant. Zones 3 and 4 are far more loaded than zone 5; however, zone 5 surpasses all the other regions in terms of torque contribution duration, accounting for more than 2/3 of the bucket period.

The radius of application of the location, where the momentum change occurs, does not seem to play a significant role in the resulting bucket torque. The most critical point is the jet energy, the surface orientation, and the trajectories of the water particles. Figure 11 shows the torque produced by the inner surfaces of the active buckets of the runner normalized by the mechanical torque measured on the experimental test rig. The mean value of the predicted torque appears to be almost 15% lower than the measured one. This is not consistent with the pressure signals results and the zone power map. This indicates that a significant fraction of the torque is produced by the backside of the bucket.

The torque contribution of the backside of one bucket is reported in Fig. 12. When the bucket first interacts with the jet, a countertorque is visible. During the jet-cutting process, the torque increases and reaches a maximum value at about 12 deg, which is about 7.5% of the torque produced by the whole inner surface of the bucket. This indicates that the backside of the bucket, in the vicinity of the cutout, behaves like the blade of a reaction turbine.

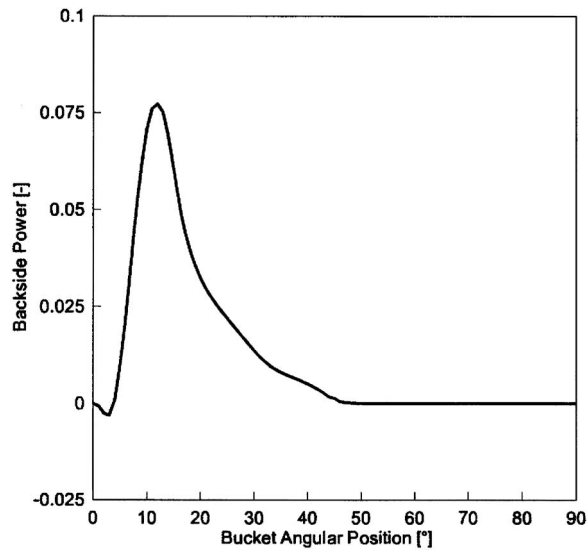


Fig. 11 Contribution to the total mechanical torque of the inner side of a single bucket as a function of the runner rotation angle. The computed values of the torque are normalized by the mean value of the measured torque.

In fact, it had been shown that a lift increase may be obtained when suitably curved convex surfaces are placed near a jet due to the Coanda effect [22–24]. Indeed, attempts were successfully made to develop reaction turbines based on a similar principle, using the deviation of a jet along a curved convex wall to drive the shaft of the machine [22,23]. The assumption of a Coanda interaction is confirmed by the experimental observations of the jet deformation and bendings (see Fig. 9).

Moreover, at some location, the numerical flow simulation results indicate very low pressures that could lead to the onset of cavitation on the machine. Indeed, some Pelton machines do exhibit erosion on the back surface, near the cutout [25,26].

Conclusions

The free surface flow in a Pelton turbine bucket is investigated by using both unsteady numerical simulations, based on the two-phase homogeneous physical model and pressure measurements

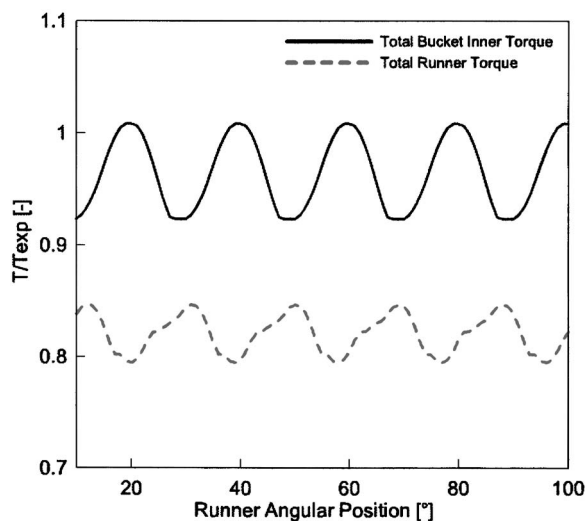


Fig. 12 Bucket backside contribution to the total mechanical power exchange as a function of the runner rotation angle. The power is normalized by the total bucket power peak value.

carried out in the buckets inner surfaces. The analysis of the results obtained allows identifying five distinct zones in the bucket inner surface. The predicted pressures match the experimental results well, especially in the zones where the flow is dominated by inertia effects and where the flow is not affected by the jet-bucket interaction. From the experiments, the jet appears to be more disturbed during the cut-in process than according to the numerical flow simulation prediction. Moreover, in the zones where the flow undergoes more shear stresses, the prediction for the signal amplitudes is less accurate. This is probably because of the standard $k-\varepsilon$ turbulence model.

The computed flow patterns exhibit good agreement with the flow visualizations during the first and last stages of the bucket cycle. Results regarding the cut jet are more difficult to assess since visualizations of this portion of the cycle are not yet available. An analysis of the power transfer in the five bucket regions shows that the outer regions, between D_1 and the cutout, contribute the most to the bucket power. These areas interact early with the jet and, thus, receive water particles with a high momentum. On the other hand, the regions located near the root of the bucket are less productive, in terms of bucket torque contribution, because of the less favorable surface orientation and radius of application.

It appears from the numerical simulation that the bucket backside does contribute to the bucket torque. This is linked with the interaction between the water jet and the bucket cutout profile. The jet appears to adhere to some extent to the bucket back, showing the presence of a Coanda effect. The Coanda effect leads to the creation of a lift force, and from that an angular momentum in the sense of rotation, contributing to the runner torque. The numerical flow simulation results show a contribution of about 7.5%. The accuracy of the prediction is difficult to assess because no experimental pressures are available for the bucket backside. Nevertheless, since the predicted average runner torque is in within 5% with the measured ones, it can be concluded that such a phenomenon exists. From an experimental point of view, the deformation of the jet observed witnesses the Coanda interaction on the bucket backside in the region of the cutout.

Further experiments would require flow visualization and pressure instrumentation of the bucket backside. Moreover, the air flow between adjacent buckets should be thoroughly investigated.

Acknowledgment

The authors would like to thank, particularly, Sonia Kvicinsky, Ph.D., for having performed the experiments used in this paper. They also would like to thank the staff members of EPFL Laboratory for Hydraulic Machines, of VATECH Hydro SA in Vevey, and the Visualization Group of the Swiss Center for Scientific Super Computing for their help and support. This work is financially supported by the Swiss Federal KTI/CTI, “Commission pour la technologie et l’innovation,” Grant No. 6139.2, and VATECH Hydro SA.

Nomenclature

- A = surface area
- α = liquid volume fraction
- B_2 = bucket inner width
- C_p = pressure coefficient,
 $C_p = p - p_{ref} / [(1/8)\rho(\omega D_1)^2]$
- \vec{C} = absolute flow velocity
- D_1 = Pelton diameter
- E = specific hydraulic energy
- ε = turbulent dissipation rate
- η = efficiency
- H = head
- k = turbulent specific kinetic energy, $k = (1/2)c_i'^2$
- κ = free surface mean curvature
- n = runner rotation frequency

\vec{n} = normal unit vector
 p = static pressure
 P = power
 Q = discharge
 \vec{r} = position vector
 \vec{T} = torque
 \vec{U} = circumferential velocity
 \vec{W} = relative flow velocity
 $\vec{\omega}$ = angular rotation speed
 φ_{B_2} = discharge coefficient, $\varphi_{B_2} = Q / [z_j (\pi B_2^2 / 4) U_1]$
 ψ = specific energy coefficient, $\psi = 2E / U_1^2$
 σ = surface tension
 rms = root-mean-square value

Subscripts

m = mixture
 n = phase number
 1 = zone 1
 2 = zone 2
 3 = zone 3
 4 = zone 4
 5 = zone 5
 α = liquid phase
 β = gas phase
 opt = reference to best efficiency point

References

- [1] Lowy, R., 1944, "Efficiency analysis of Pelton Wheels," *Trans. ASME*, **66**, pp. 527–538.
- [2] Bachmann, P., Schärer, Ch., Staubli, T., and Vulllioud, G., 1990, "Experimental Flow Studies on a 1-Jet Model Turbine Pelton," *Proceedings of 15th IAHR Symposium on Modern Technology in Hydraulic Energy Production*, Sept. 11–14, Belgrade, Yugoslavia, Faculty of Mechanical Engineering, Belgrade, pp. 1–13.
- [3] Grozev, G., Obretenov, V., and Trifonov, T., 1988, "Investigation of the Distribution of Pressure Over the Buckets of a Pelton Turbine," *Proceedings of the Conference on Hydraulic Machinery and Flow Measurements*, Sept. 13–15, Ljubljana, Yugoslavia, Turboinstitut, Ljubljana, pp. 119–125.
- [4] Kvicinsky, S., Kueny, J.-L., and Avellan, F., 2002, "Numerical and Experimental Analysis of Free Surface Flows in a 3D Non-Rotating Pelton Bucket," *The 9th International Symposium on Transport Phenomena and Dynamic Rotating Machinery*, Feb. 10–14, Honolulu.
- [5] Guilbaud, M., Houdeline, J. B., and Philibert, R., 1992, "Study of the Flow in the Various Sections of a Pelton Turbine," *Proceedings of 16th IAHR Symposium on Hydraulic Machinery and Cavitation*, Sept. 14–19, São Paulo, Associação Brasileira de Recursos Hídricos, São Paulo, pp. 819–831.
- [6] Kvicinsky, S., Longatte, F., Avellan, F., and Kueny, J.-L., 1999, "Free Surface Flows: Experimental Validation of the Volume of Fluid (VOF) Method in the Plane Wall Case," *Proceedings of 3rd ASME/JSME*, San Francisco, ASME, New York, pp. 1–8.
- [7] Hana, M., 1998, "A Discussion on Numerical Simulation in Pelton Turbines," *Proceedings of 19th IAHR Symposium*, Sept. 9–11, Singapore, World Scientific, Singapore, pp. 306–315.
- [8] Sick, M., Keck, H., Parkinson, E., and Vulllioud, G., 2000, "New Challenges in Pelton Research," *Hydro 2000 Conference*, Bern, Switzerland.
- [9] Parkinson, P., Garcin, H., Bissel, C., Muggli, F., and Braune, A., 2002, "Description of Pelton Flow Patterns With Computational Flow Simulations," *Hydro 2002: Development, Management, Performances*, Nov. 4–7, Kiris, Turkey.
- [10] Parkinson, E., Vulllioud, G., Geppert, L., and Keck, H., 2002, "Analysis of Pelton Turbine Flow Patterns for Improved Runner-Component Interaction," *Int. J. Hydropow. Dams*, **1**(5), pp. 100–103.
- [11] Janetzky, B., Göde, E., Ruprecht, A., Keck, H., and Schärer, Ch., 1998, "Numerical Simulation of the Flow in a Pelton Bucket," *Proceedings of 19th IAHR Symposium*, Sept. 9–11, Singapore, World Scientific, Singapore, pp. 276–284.
- [12] Mack, R., and Moser, W., 2002, "Numerical Investigations of the Flow in a Pelton Turbine," *Proceedings of XXIst IAHR Symposium on Hydraulic Machinery and Systems*, Sept. 9–12, Lausanne, Laboratory for hydraulic machines, Lausanne, pp. 373–378.
- [13] Kvicinsky, S., Kueny, J.-L., Avellan, F., and Parkinson, E., 2002, "Experimental and Numerical Analysis of Free Surface Flows in a Rotating Bucket," *Proceedings of XXIst IAHR Symposium on Hydraulic Machinery and Systems*, Sept. 9–12, Lausanne, Laboratory for Hydraulic Machines, Lausanne, pp. 359–364.
- [14] Farhat, M., Natal, S., Avellan, F., Paquet, F., Lowys, P., and Couston, M., 2002, "Onboard Measurements and Strain Fluctuations in a Model of Low Head Francis Turbine, Part I: Instrumentation," *Proceedings of the XXIst IAHR Symposium on Hydraulic Machinery and Systems*, Sept. 9–12, Lausanne, Laboratory for hydraulic machines, Lausanne, pp. 865–871.
- [15] Ishii, M., 1975, "Thermo-Fluid Dynamic Theory of Two-Phase Flow," *Collection de la Direction des Etudes et Recherches*, EDF, Eyrolles, Paris, pp. 1–248.
- [16] Zwart, P. J., Scheuerer, M., and Bogner, M., 2003, "Free Surface Flow Modeling of an Impinging Jet," *ASTAR International Workshop on Advanced Numerical Methods for Multidimensional Simulation of Two-Phase Flow*, Sept. 15–16, GRS Garching, Germany.
- [17] Brackbill, J. U., Kothe, D. B., and Zemach, C., 1992, "A Continuum Method for Modeling Surface Tension," *J. Comput. Phys.*, **100**, pp. 335–354.
- [18] Perrig, A., Farhat, M., Avellan, F., Parkinson, E., Garcin, H., Bissel, C., Valle, M., and Favre, J., 2004, "Numerical Flow Analysis in a Pelton Turbine Bucket," *Proceedings of 22nd IAHR Symposium on Hydraulic Machinery and Systems*, June 29–July 2, Stockholm, Swedpower, Stockholm, pp. A10-3-1–A10-3-14.
- [19] Ténoc, A., 1930, *Turbines Hydrauliques et Régulateurs Automatiques de Vitesse*, Vols. I & II, Librairie de l'Enseignement Technique, Eyrolles, Paris.
- [20] Webster, J., 1971, "Analysis of Jet-Type Impulse Turbines," *Water Power*, **23**, pp. 287–292.
- [21] Johnson, W., and Vickers, G. W., 1973, "Transient Stress Distribution Caused by Water-Jet Impact," *J. Mech. Eng. Sci.*, **15**(4), pp. 302–310.
- [22] Wille, R., and Fernholz, H., 1965, "Report on the First European Mechanics Colloquium on the Coanda Effect," *J. Fluid Mech.*, **23**, pp. 801–819.
- [23] Teodorescu-Tintea, C., 1967, "On a New Functional Principle in the Theory of Gas Turbines Based on the Coanda Effect: The Turbine Fitted With Depressive Blades," *Rev. Roum. Sci. Tech., Ser. Mec. Appl.*, **12**(1), pp. 85–101.
- [24] Fujisawa, N., and Shirai, H., 1987, "Experimental Investigation of the Unsteady Flow Field Around a Savonius Rotor at Maximum Power Performance," *Wind Eng.*, **11**(4), pp. 195–206.
- [25] Grein, H., 1990, "Cavitation Pitting and Rain Erosion on Pelton Runners," *Proceedings of 15th IAHR Symposium on Modern Technology in Hydraulic Energy Production*, Sept. 11–14, Belgrade, Yugoslavia, pp. 1–9.
- [26] Brivio, R., and Zappi, O., 1995, "La Cavitazione Nelle Turbine Pelton (Parte I)," *Energ. Elettr.*, **72**(2), pp. 45–49.